

# Chemical Science

rsc.li/chemical-science



ISSN 2041-6539



## EDGE ARTICLE

Jinlong Gong *et al.*

Achieving convenient CO<sub>2</sub> electroreduction and photovoltage in tandem using potential-insensitive disordered Ag nanoparticles

Cite this: *Chem. Sci.*, 2018, 9, 6599

All publication charges for this article have been paid for by the Royal Society of Chemistry

# Achieving convenient CO<sub>2</sub> electroreduction and photovoltage in tandem using potential-insensitive disordered Ag nanoparticles†

Wanyu Deng,<sup>‡</sup> Lei Zhang,<sup>‡</sup> Hao Dong,<sup>‡</sup> Xiaoxia Chang, Tuo Wang<sup>‡</sup> and Jinlong Gong<sup>‡</sup>\*

Photovoltaic-electrochemical (PV-EC) systems can not only make full use of solar energy, but also transform CO<sub>2</sub> into organic molecules. However, it is difficult to achieve PV-EC systems since most CO<sub>2</sub> reduction catalysts are potential-dependent. This paper describes the rational design of potential-insensitive disordered Ag, which can achieve more than 90% faradaic efficiency (FE) for CO within a wide voltage range of 1.1 V in an electroreduction CO<sub>2</sub> system. The system shows attractive activity under different photovoltage conditions in a PV-EC system. By employing *in situ* attenuated total reflection surface-enhanced infrared absorption spectroscopy (ATR-SEIRAS), we address the origin of the volcano peak of FE on Ag nanoclusters to understand the mechanism of the carbon dioxide reduction reaction (CO<sub>2</sub>RR). In addition, we find that the CO<sub>2</sub>RR on disordered Ag nanoparticles is a proton–electron coupling transfer (PECT) reaction mechanism, which may result in high activity in a wide potential range.

Received 12th June 2018

Accepted 19th July 2018

DOI: 10.1039/c8sc02576b

rsc.li/chemical-science

CO<sub>2</sub> in the atmosphere has recently reached the highest levels in human history due to the huge consumption of fossil fuels.<sup>1,2</sup> Previous work showed that CO<sub>2</sub> conversion to fuels and chemical feedstock could be achieved through electrochemical,<sup>1</sup> photochemical,<sup>3</sup> photoelectrochemical,<sup>4</sup> thermochemical,<sup>5</sup> and photovoltaic-electrochemical (PV-EC)<sup>6–9</sup> routes. Among these approaches, the PV-EC system has several advantages, such as potential large-scale amplification due to the modular electrolyzer design and ease of integration with solar energy sources. Therefore, the utilization of electrical energy generated by photovoltage to drive the electrochemical CO<sub>2</sub>RR to yield fuel and chemical feedstock is feasible and of great prospect.<sup>6–9</sup> However, it has been reported that the distribution of CO<sub>2</sub>RR products is potential-dependent.<sup>10–13</sup> Hence, CO<sub>2</sub>RR coupled components need to be carefully selected. Meanwhile, under actual operation conditions, the fickle change of sunlight intensity can also affect the photogenerated voltage. Therefore, it is important and necessary to design a potential-insensitive catalyst with high efficiency and selectivity.

To achieve a PV-EC system, selection of the catalyst is also a key factor since the activity and selectivity of the electrocatalyst have a great effect on system efficiency and product

distribution. Among various types of electrocatalysts, Au, Ag, Zn, and Pd are known to produce carbon monoxide (CO) with varying faradic efficiency, which depend on the potential.<sup>10,14–16</sup> Meanwhile, Au and Ag based catalysts exhibit the highest activity and selectivity towards CO during the electrocatalytic CO<sub>2</sub> reduction process. Since Ag is much more abundant and less expensive than Au, it is considered as the more promising electrocatalyst for large-scale production of CO. Hwang and co-workers investigated the relationship between the particle size of Ag nanoparticles and CO<sub>2</sub>RR activity.<sup>10</sup> Subsequently, Luo and co-workers combined experimental and computational efforts to propose that CO<sub>2</sub>RR activity and selectivity on Ag could be greatly promoted by creating optimal facets and edge sites.<sup>17</sup> However, almost all the Ag catalysts showed an apparent volcano peak with potential during the CO<sub>2</sub>RR process, and the potential window for optimal activity is too narrow for a PV-EC system, which limits the large-scale utilization of catalysts in the solar-driven electrochemical CO<sub>2</sub>RR.

This paper describes the discovery of disordered Ag nanoparticles on a carbon support catalyst, which could achieve 90% FE for CO in a wide voltage range instead of showing an apparent volcano peak. In order to test the superiority of the potential-insensitive catalyst, a new PV-EC system was fabricated firstly with the disordered Ag catalyst, Pt foil and a six-section a-Si solar cell as the cathode, anode and photovoltage source, respectively. It was found that the disordered Ag nanoparticles showed attractive and potential-insensitive activity. Finally, by using ATR-SEIRAS spectra, the CO<sub>2</sub>RR mechanism and the relationship between CO FE and potential over Ag nanoparticles were explained.

Key Laboratory for Green Chemical Technology of Ministry of Education, School of Chemical Engineering and Technology, Tianjin University, Collaborative Innovation Center of Chemical Science and Engineering, Tianjin 300072, China. E-mail: jlgong@tju.edu.cn

† Electronic supplementary information (ESI) available. See DOI: 10.1039/c8sc02576b

‡ These two authors contributed equally to this work.

A series of carbon-supported Ag nanoparticles were prepared. The disordered particle size Ag was controlled by adjusting the stirring speed and heating rate. Meanwhile, the uniform particle diameter Ag was synthesized by adjusting the reaction time and Ag precursor species (see the ESI† for experimental details).<sup>10</sup> Fig. 1a shows that the disordered Ag size distribution is irregular, while uniform Ag (Fig. 1b–d) size distributions are  $3.2 \pm 0.05$  nm,  $4.9 \pm 0.04$  nm, and  $11.0 \pm 0.1$  nm, respectively. The *d*-spacing of all the Ag nanoparticles is 0.23 nm which corresponds to the Ag (111) crystal plane (Fig. 1e–h). It can also be found that these nanoparticles have a face-centered cubic Ag crystal structure from the X-ray diffraction (XRD) data in Fig. S1.†

To test the CO<sub>2</sub>RR performances on Ag nanoparticles, controlled potential electrolysis of CO<sub>2</sub> was performed in a three-electrode system (Fig. S2a†). Under the test conditions, CO FE of uniform Ag nanoparticles and Ag foil shows a volcano peak with potential dependence (Fig. 2a) in 0.1 M KHCO<sub>3</sub>, wherein the HER is facile at low overpotentials and CO<sub>2</sub>RR is prone to occur with increased potential, while CO FE decreases at higher potentials. On 3 nm, 5 nm and 11 nm Ag, maximum efficiencies of 83%, 90% and 95% are achieved at −1.1, −0.6 and −1.4 V, respectively. Interestingly, CO FE of disordered Ag is more than 90% from −0.6 V to −1.7 V. The highest CO FE is close to 70% at −1.3 V over Ag foil, which matches well with the previous work.<sup>18</sup> To rule out the influence of the electrolyte, we

tested CO<sub>2</sub>RR in 0.1 M KCl (Fig. 2b). The activity of Ag catalysts is not affected by KCl electrolyte. In contrast, the performance is slightly better because of the Cl<sup>−</sup> adsorbed on the electrode surface inhibiting the HER.<sup>19,20</sup>

It should be noted that achieving such a wide voltage range of CO<sub>2</sub>RR activity is difficult, even by mixing 3, 5, 11 nm Ag in the mass ratio of 1 : 1 : 1. It might be attributed to the uneven distribution of Ag particles on the glassy carbon electrode surface. When the same ink was tested five times (Fig. 2c), a simple mixture of 3–5–11 nm Ag showed a much larger error bar than disordered Ag or 5 nm Ag, which proved that the performance of mixed 3–5–11 nm Ag exposed to the glassy carbon electrode surface is different for the five times. Therefore, it is hard to achieve potential-insensitive activity by mechanically mixing different particle size Ag nanoparticles.

The current density for CO increases with potential on disordered Ag (Fig. 2d), indicating accelerated reaction rate for CO<sub>2</sub> reduction and it is maintained at  $-16.7 \text{ mA cm}^{-2}$ , which is probably caused by the limited mass transport of CO<sub>2</sub> in 0.1 M KHCO<sub>3</sub> solution.<sup>21,22</sup> However, the current density of uniform Ag decreases at a higher potential. A durability test was performed with Ag foil and disordered Ag for five hours at −1.1 V (the best potential for CO<sub>2</sub>RR on Ag foil) and −0.7 V, respectively. Although the current density is stable for both Ag foil and disordered Ag during the 5 hour test, the decline of FE for CO on disordered Ag is 16.0% compared to 54.3% on Ag foil (Fig. S3a



Fig. 1 Transmission electron microscopy images and histograms of particle-size distribution of (a and e) disordered, (b and f) 3 nm, (c and g) 5 nm and (d and h) 11 nm Ag on a carbon support.







Fig. 2 CO faradaic efficiency depending on applied potential in CO<sub>2</sub> saturated (a) 0.1 M KHCO<sub>3</sub> and (b) 0.1 M KCl, (c) CO faradaic efficiency on a simple mixture of 3–5–11 nm, disordered and 5 nm Ag in 0.1 M KHCO<sub>3</sub> with error bars. (d) CO partial current density depending on applied potential.

and b<sup>†</sup>). It shows that disordered Ag is much more stable than Ag foil.<sup>10</sup> From the TEM (Fig. S4<sup>†</sup>) and X-ray photoelectron spectra (XPS, Fig. S5<sup>†</sup>) after 5 hours CO<sub>2</sub>RR, the overall morphology of Ag nanoparticles remains unchanged and the Ag 3d peak is basically the same. To compare with previous electrocatalysts for the CO<sub>2</sub> reduction to CO, the activity data are summarized in Table S1 and Fig. S6.<sup>†</sup> Disordered Ag shows a very competitive FE for CO as well as the widest voltage range at the FE higher than 90%.

Further, solar-driven CO<sub>2</sub> reduction was performed in an H-cell filled with 0.1 M KHCO<sub>3</sub> solution (Fig. S2b<sup>†</sup>). Before the PV-EC system test, it is necessary to determine how much light induced voltage is needed to drive both CO<sub>2</sub>RR and oxygen evolution reaction (OER). The linear sweep voltammetry measurements were conducted on disordered Ag and Pt foil in 0.1 M KHCO<sub>3</sub>. As deduced from Fig. 3a, a voltage of 2.4 V was required. At the same time, a six-section a-Si with an area of 25 cm<sup>2</sup> can provide an open circuit voltage of 3.38 V and a short circuit current of 4.6 mA cm<sup>-2</sup>, which can meet the demand of the CO<sub>2</sub>RR and photovoltage in tandem (Fig. 3b). During the PV-EC system test, a potential of -0.75 V can be observed at the cathode (Fig. 3c). Through product analysis it was found that the disordered Ag exhibits the highest CO FE of 92.7%, while 3 nm, 5 nm and 11 nm Ag can only achieve 48.0%, 87.2% and 68.2%, respectively (Fig. 3d), which is consistent with the previous measurement results at -0.75 V in a three-electrode system (Fig. 2a). It should be noted that the selection of photovoltage was limited to the cathode potential. To further

illustrate that the potential-insensitive disordered Ag is the best choice for the tandem cell, a ten-section random sheltered a-Si solar cell is used. Fig. S7a<sup>†</sup> shows that the cathode potential is about -1.0 V using a ten-section a-Si solar cell. The disordered Ag exhibits the best activity of 91.8% and the FE for CO of 3 nm, 5 nm and 11 nm Ag are 60.1%, 45.1% and 74.3% (Fig. S7b<sup>†</sup>), respectively. Even when the area of the twelve-section a-Si solar cell changes randomly (Fig. S7c<sup>†</sup>), the disordered Ag still exhibits the best activity of 92.8% and the FE for CO of 3 nm, 5 nm and 11 nm Ag turn into 79.9%, 71.3% and 25.3% (Fig. S7d<sup>†</sup>), respectively. In the PV-EC system, it is difficult for the output voltage of practical solar cells under sunlight to remain stable and achieve a specific cathode potential. Fortunately, the disordered Ag is potential-insensitive and thus CO FE will not be affected with changing potential. The durability test with disordered Ag in the PV-EC system was also conducted, in which the decline of FE for CO was close to that of the three electrode system (16.8%) for five hours (Fig. S3c<sup>†</sup>). It can be speculated that enhancement in the stability of the PV-EC system could be achieved by improving the stability of the cathode catalyst. At the same time, the decline of FE for CO on 3 nm, 5 nm, 11 nm Ag nanoparticles is almost the same as in the case of uniform Ag catalysts (Fig. S3d–f<sup>†</sup>), which could be determined by the catalyst preparation method. Due to the low short circuit current (4.6 mA cm<sup>-2</sup>) of the commercially purchased a-Si solar cell caused by excessive series, the solar to cathode product (STC) efficiency of our PV-EC system is 0.1% (see the ESI<sup>†</sup> for further detailed calculations).





Fig. 3 (a) Performance of the disordered Ag and Pt film towards the CO<sub>2</sub>RR and OER by linear sweep voltammetry at a scan rate of 50 mV s<sup>-1</sup> in 0.1 M KHCO<sub>3</sub>. (b) The current density–voltage characteristics of a six-section a-Si solar cell were measured under AM 1.5G illumination. (c) Cathode voltage and (d) CO FE in the PV-EC system driven by a six-section a-Si solar cell.

From a thermodynamic perspective, the free energy diagram (Fig. S8†) indicates the competitive relationships between the CO<sub>2</sub>RR and HER on the Ag surface at different potentials.<sup>17,23</sup> When a potential of 0 V is applied (purple line), the formation of \*COOH for the CO<sub>2</sub>RR and that of \*H for the HER are still uphill energy barriers, which are about -1.2 eV and -0.8 eV, respectively. At this stage, neither the CO<sub>2</sub>RR nor the HER can happen. With the increase of potential to -0.8 V (green line), the energy barrier for the HER can be overcome, but it is still not achieved for the CO<sub>2</sub>RR. As a result, the HER takes place and causes low CO FE at low potential. When the energy barrier for the CO<sub>2</sub>RR is overcome (-1.2 V, red line), the CO<sub>2</sub>RR starts to occur and CO FE increases (Fig. 2a). When the potential exceeds a specific value, the CO<sub>2</sub>RR dominates. For example, at -1.6 V (blue line), a much lower energy barrier of the CO<sub>2</sub>RR is obtained compared with the HER. From a dynamic point of view, the Tafel slopes of disordered or uniform Ag and Ag foil are close to 128 mV dec<sup>-1</sup> (Fig. S9†), which indicates that one electron transfer is the rate-determining step for these catalysts.<sup>24</sup> It is worth noting that the two electron transfer processes are involved in the formation of \*CO for the CO<sub>2</sub>RR, while only one electron is needed for the HER. Even if it requires two \*H to form H<sub>2</sub>, it only takes one electron to form \*H. Hence, the CO<sub>2</sub>RR is more sensitive to potential, because the potential energy of electrons changes with cathode potential. For example, if two electrons are required for an elementary reaction step, the barrier of the reaction increases by -2 eV when the potential of -1 V is increased. Thus, more electron transfer steps would be more sensitive to potentials. By rights, CO FE and partial density

current should increase with potential until mass transfer control is achieved. However, the uniform Ag catalyst shows a volcano peak of CO FE (Fig. 2a), which may suggest a change in mechanism with potential. It is noteworthy that the Tafel slope can only suggest the reaction process under low potential.

To understand the CO<sub>2</sub> reduction reaction process on Ag nanoparticles, the ATR-SEIRAS spectra were used to observe the intermediate process (see the ESI† for experimental details). According to Fig. 4a, the peak at 1650 cm<sup>-1</sup> is the overlays of H-O-H bending and C=O asymmetric stretching (1660 cm<sup>-1</sup>) of \*COOH.<sup>25–27</sup> The peak at 1378 cm<sup>-1</sup> belongs to symmetric \*COO<sup>-</sup> stretching and C-O stretching.<sup>28</sup> Other absorptions appearing at 1290 cm<sup>-1</sup> can be ascribed to the C-OH stretch of \*COOH.<sup>25,26</sup> Therefore, the formation of the \*COOH intermediate from 1378 cm<sup>-1</sup> and 1290 cm<sup>-1</sup> and the formation of \*COO<sup>-</sup> intermediate by comparing their peak strengths can be extrapolated. The detail band assignments are shown in Table S2.† To rule out the influence of the Au substrate and Ag-C catalyst itself, the Au substrate was recorded in CO<sub>2</sub> saturated 0.1 KCl electrolyte and the disordered Ag catalyst was recorded in Ar saturated 0.1 KCl electrolyte, respectively. No absorbance was observed from 1400–1270 cm<sup>-1</sup> at different applied potential (Fig. S10†).

In Fig. 4b, the ATR-SEIRAS spectra were recorded on 3 nm Ag at -0.5, -0.9, -1.1 and -1.5 V. The clear difference in the spectrum is that the 1378 cm<sup>-1</sup> peak is larger than the 1290 cm<sup>-1</sup> peak at -1.1 V and -1.5 V, indicating the coupling of C-O stretch of \*COOH and the symmetric stretch of \*COO<sup>-</sup>. However, the 1378 cm<sup>-1</sup> peak is hard to be observed at -0.5 V



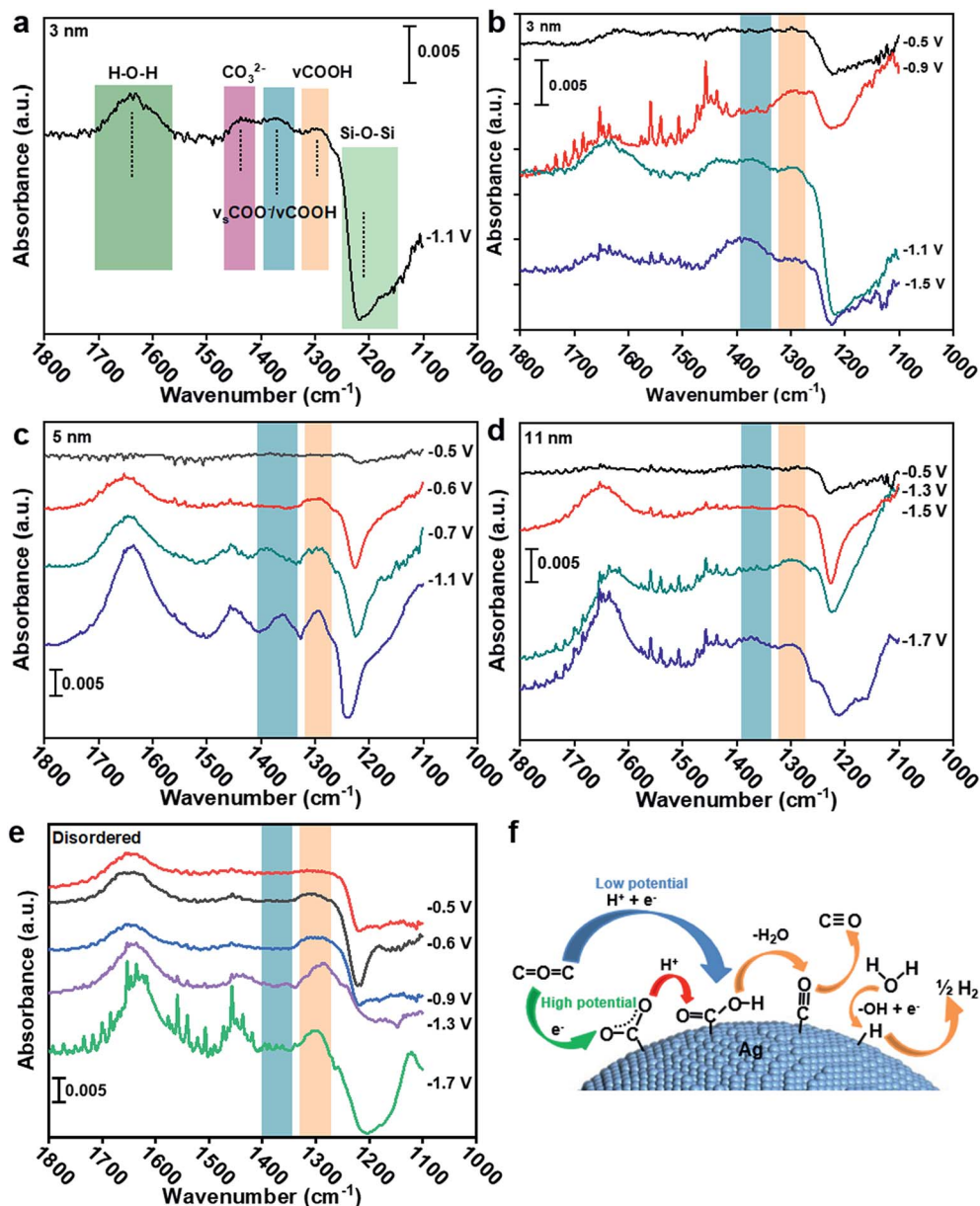


Fig. 4 (a) ATR-SEIRAS spectra of 3 nm Ag in  $\text{CO}_2$  saturated 0.1 M KCl electrolyte at  $-1.1$  V. ATR-SEIRAS spectra of (b) 3 nm, (c) 5 nm, (d) 11 nm and (e) disordered Ag in  $\text{CO}_2$  saturated 0.1 M KCl electrolyte at different potentials. (f) Reaction mechanism for the  $\text{CO}_2$ RR and HER on the Ag surface.

and  $-0.9$  V, despite the obvious occurrence of the  $1290\text{ cm}^{-1}$  peak at  $-0.9$  V, implying no sign of the  $\text{COO}^*$  intermediate. It can be indicated that the  $\text{CO}_2$ RR on 3 nm Ag is a proton-electron coupling transfer (PECT) process at low potential ( $< -0.9$  V, Fig. 4f). However, at high potential ( $> -1.1$  V), the reaction mechanism changes, in which an electron first transfers to form  $\text{COO}^*$  and then a proton is introduced to form  $\text{COOH}^*$  (Fig. 4f),<sup>28</sup> which is a rate-limiting step for the  $\text{CO}_2$ RR.<sup>23</sup> Since the rate-limiting step is not electron transfer, the  $\text{CO}_2$ RR would not be affected by potential. Therefore, CO FE begins to decrease and shows a volcano peak. The decrease of CO current density (Fig. 2d) is because of the competition between the  $\text{CO}_2$ RR and HER; as more protons participate in the HER process, it will be difficult for  $\text{COO}^*$  to accept protons

generating  $\text{COOH}^*$ . For 5 nm and 11 nm Ag (Fig. 4c and d),  $\text{COO}^*$  can only be found at potentials higher than  $-0.7$  V and  $-1.5$  V, respectively. Hence, the trigger potentials for 3 nm, 5 nm and 11 nm Ag are  $-1.1$  V,  $-0.7$  V and  $-1.5$  V, respectively, which are very close to the potentials of the best CO FE  $-1.1$  V,  $-0.6$  V and  $-1.4$  V (Fig. 2a). For disordered Ag, the peak at  $1378\text{ cm}^{-1}$  is less obvious than that at  $1290\text{ cm}^{-1}$  at five tested potentials, indicating no sign of the  $\text{COO}^*$  intermediate or a trigger potential from  $-0.5$  V to  $-1.7$  V (Fig. 4e). It shows that the  $\text{CO}_2$ RR on disordered Ag is a PECT process (Fig. 4f), where the  $\text{CO}_2$ RR can be promoted with the increase of potential against the HER. As a result, there is no volcano peak of CO FE on disordered Ag.



In summary, disordered Ag catalysts with considerably high activity in a wide voltage range instead of showing a volcano peak were successfully synthesized. From the solar-driven CO<sub>2</sub> reduction experiment, the disordered Ag can achieve efficient CO<sub>2</sub> reduction under different photovoltage conditions. By using ATR-SEIRAS, it can be found that disordered Ag undergoes the PECT process with increasing potentials. By contrast, the PECT process on uniform Ag changes to an electron-proton separated transfer process at high potential. In a wider PV-EC system context, the rational design of the potential-insensitive Ag catalyst for PV-EC CO<sub>2</sub> reduction can inspire the design of other potential-insensitive CO<sub>2</sub>RR electrocatalysts for production of HCOOH, CH<sub>4</sub>, CH<sub>3</sub>OH, etc.

## Conflicts of interest

There are no conflicts to declare.

## Acknowledgements

We acknowledge the National Key R&D Program of China (2016YFB0600901), the National Natural Science Foundation of China (U1463205, 21525626, and 21606169), and the Program of Introducing Talents of Discipline to Universities (B06006) for financial support. We also would like to express our gratitude to all those who helped us to build the ATR-SEIRAS device, including Prof. Bingjun Xu (Department of Chemical and Biomolecular Engineering, University of Delaware) and Prof. Wenbin Cai (Shanghai Key Laboratory of Molecular Catalysis and Innovative Materials, Institute of New Energy, Fudan University).

## References

- 1 L. Zhang, Z. J. Zhao and J. Gong, *Angew. Chem., Int. Ed.*, 2017, **56**, 11326–11353.
- 2 D. D. Zhu, J. L. Liu and S. Z. Qiao, *Adv. Mater.*, 2016, **28**, 3423–3452.
- 3 X. Chang, T. Wang and J. Gong, *Energy Environ. Sci.*, 2016, **9**, 2177–2196.
- 4 S. Xie, Q. Zhang, G. Liu and Y. Wang, *Chem. Commun.*, 2016, **52**, 35–59.
- 5 A. Goepfert, M. Czaun, J. P. Jones, G. S. Prakash and G. A. Olah, *Chem. Soc. Rev.*, 2014, **43**, 7995–8048.
- 6 M. Aresta, A. Dibenedetto and A. Angelini, *Chem. Rev.*, 2014, **114**, 1709–1742.
- 7 E. V. Kondratenko, G. Mul, J. Baltrusaitis, G. O. Larrazábal and J. Pérez-Ramírez, *Energy Environ. Sci.*, 2013, **6**, 3112.
- 8 F. Urbain, P. Tang, N. M. Carretero, T. Andreu, L. G. Gerling, C. Voz, J. Arbiol and J. R. Morante, *Energy Environ. Sci.*, 2017, **10**, 2256–2266.
- 9 J. Bullock, D. F. Srankó, C. M. Towle, Y. Lum, M. Hettick, M. Scott, A. Javey and J. Ager, *Energy Environ. Sci.*, 2017, **10**, 2222–2230.
- 10 C. Kim, H. S. Jeon, T. Eom, M. S. Jee, H. Kim, C. M. Friend, B. K. Min and Y. J. Hwang, *J. Am. Chem. Soc.*, 2015, **137**, 13844–13850.
- 11 C. W. Li and M. W. Kanan, *J. Am. Chem. Soc.*, 2012, **134**, 7231–7234.
- 12 S. Sarfraz, A. T. Garcia-Esparza, A. Jedidi, L. Cavallo and K. Takanabe, *ACS Catal.*, 2016, **6**, 2842–2851.
- 13 J. Wu, R. M. Yadav, M. Liu, P. P. Sharma, C. S. Tiwary, L. Ma, X. Zou, X. D. Zhou, B. I. Yakobson and J. Lou, *ACS Nano*, 2015, **9**, 5364–5371.
- 14 W. Zhu, Y. J. Zhang, H. Zhang, H. Lv, Q. Li, R. Michalsky, A. A. Peterson and S. Sun, *J. Am. Chem. Soc.*, 2014, **136**, 16132–16135.
- 15 H. Won da, H. Shin, J. Koh, J. Chung, H. S. Lee, H. Kim and S. I. Woo, *Angew. Chem., Int. Ed.*, 2016, **55**, 9297–9300.
- 16 D. Gao, H. Zhou, J. Wang, S. Miao, F. Yang, G. Wang, J. Wang and X. Bao, *J. Am. Chem. Soc.*, 2015, **137**, 4288–4291.
- 17 S. Liu, H. Tao, L. Zeng, Q. Liu, Z. Xu, Q. Liu and J. L. Luo, *J. Am. Chem. Soc.*, 2017, **139**, 2160–2163.
- 18 T. Hatsukade, K. P. Kuhl, E. R. Cave, D. N. Abram and T. F. Jaramillo, *Phys. Chem. Chem. Phys.*, 2014, **16**, 13814–13819.
- 19 Y. C. Hsieh, S. D. Senanayake, Y. Zhang, W. Xu and D. E. Polyansky, *ACS Catal.*, 2015, **46**, 2584–2592.
- 20 A. S. Varela, W. Ju, T. Reier and P. Strasser, *ACS Catal.*, 2016, **6**, 2136–2144.
- 21 S. Ma and P. J. Kenis, *Curr. Opin. Chem. Eng.*, 2013, **2**, 191–199.
- 22 A. Kahyarian, M. Singer and S. Nesic, *J. Nat. Gas Sci. Eng.*, 2016, **29**, 530–549.
- 23 M. R. Singh, J. D. Goodpaster, A. Z. Weber, M. Head-Gordon and A. T. Bell, *Proc. Natl. Acad. Sci. U. S. A.*, 2017, **114**, E8812–E8821.
- 24 K. Heusler, *Berichte der Bunsengesellschaft für physikalische Chemie*, 1994, vol. 98, pp. 644–645.
- 25 S. J. Lee, S. W. Han, M. Yoon and K. Kim, *Vib. Spectrosc.*, 2000, **24**, 265–275.
- 26 E. Garand, T. Wende, D. J. Goebbert, R. Bergmann, G. Meijer, D. M. Neumark and K. R. Asmis, *J. Am. Chem. Soc.*, 2009, **132**, 849–856.
- 27 S. W. Han, T. H. Ha, C. H. Kim and K. Kim, *Langmuir*, 1998, **14**, 6113–6120.
- 28 N. J. Firet and W. A. Smith, *ACS Catal.*, 2016, **7**, 606–612.

